



**HAL**  
open science

# Cross-field electron diffusion due to the coupling of drift-driven microinstabilities

Kentaro Hara, Sedina Tsikata

► **To cite this version:**

Kentaro Hara, Sedina Tsikata. Cross-field electron diffusion due to the coupling of drift-driven microinstabilities. *Physical Review E*, 2020, 102 (2), pp.023202. 10.1103/PhysRevE.102.023202. hal-02917882


**HAL Id: hal-02917882**

**<https://hal.science/hal-02917882>**

Submitted on 7 Jan 2021

**HAL** is a multi-disciplinary open access archive for the deposit and dissemination of scientific research documents, whether they are published or not. The documents may come from teaching and research institutions in France or abroad, or from public or private research centers.

L'archive ouverte pluridisciplinaire **HAL**, est destinée au dépôt et à la diffusion de documents scientifiques de niveau recherche, publiés ou non, émanant des établissements d'enseignement et de recherche français ou étrangers, des laboratoires publics ou privés.

**Cross-field electron diffusion due to the coupling of drift-driven microinstabilities**Kentaro Hara <sup>\*</sup>*Department of Aeronautics and Astronautics, 496 Lomita Mall, Stanford University, Stanford, California 94305, USA*Sedina Tsikata <sup>†</sup>*ICARE UPR 3021, Centre National de la Recherche Scientifique (CNRS), Orléans, France*

(Received 29 December 2019; revised 23 May 2020; accepted 10 July 2020; published xxxxxxxxx)

In this paper, the nonlinear interaction between kinetic instabilities driven by multiple ion beams and magnetized electrons is investigated. Electron diffusion across magnetic field lines is enhanced by the coupling of plasma instabilities. A two-dimensional collisionless particle-in-cell simulation is performed accounting for singly and doubly charged ions in a cross-field configuration. Consistent with prior linear kinetic theory analysis and observations from coherent Thomson scattering experiments, the present simulations identify an ion-ion two-stream instability due to multiply charged ions (flowing in the direction parallel to the applied electric field) which coexists with the electron cyclotron drift instability (propagating perpendicular to the applied electric field and parallel to the  $E \times B$  drift). Small-scale fluctuations due to the coupling of these naturally driven kinetic modes are found to be a mechanism that can enhance cross-field electron transport and contribute to the broadening of the ion velocity distribution functions.

DOI: [10.1103/PhysRevE.00.003200](https://doi.org/10.1103/PhysRevE.00.003200)**I. INTRODUCTION**

Electron diffusion across magnetic field lines plays an important role in a variety of contexts, including fusion, astrophysical, ionospheric, and cross-field plasma discharges. Partially magnetized plasmas, where ions are nonmagnetized and electrons are magnetized, exhibit enhanced electron mobility, i.e., reduced electron confinement, in the direction across the magnetic field lines [1,2]. Plasma turbulence is of critical importance for understanding transport of charged species [3]. A number of key kinetic instabilities have been investigated in the literature in the context of electron transport, including, but not limited to, the electron cyclotron drift instability (ECDI) [4–8], modified two-stream instability (MTSI) [9,10], and ion acoustic instability (IAI) [11–13].

Although electron diffusion across the magnetic field lines can be caused by a plasma wave in the  $E \times B$  direction, microturbulence may be driven not only by one type of linear instability but by the nonlinear interaction of multiple linear instabilities [14]. In a laboratory cross-field discharge, theoretical and numerical studies identified the plasma waves driven by the ECDI [15–17] and these results were subsequently supported by coherent Thomson scattering experiments [18–21]. In recent years, an increasing number of numerical studies have been undertaken by several groups revisiting this instability [22–26] and its role in transport.

One of the key experimental results in Ref. [20] was the detection of a plasma wave in the cross-field direction (parallel to the applied electric field), exhibiting a spatial scale similar

to that of the ECDI observed primarily in the  $E \times B$  direction. Subsequent linear kinetic theory analyses revealed that such cross-field oscillations observed in experiments can be initiated by the ion-ion two-stream instability (IITSI) [27–31] due to the presence of singly and doubly charged ion streams. Generally, mode coupling of different instability mechanisms plays an important role in plasma transport, particularly in the nonlinear saturation phase of instabilities. However, it is difficult to evaluate the effects of such mode coupling on electron transport, e.g., current density, using diagnostic tools or linear theories. The linear growth rate denotes how *fast* an instability develops but does not account for how large its amplitude ultimately becomes, i.e., at what level the nonlinear saturation occurs. High-fidelity plasma simulations are therefore of critical importance to investigate nonlinear dynamics of coupled plasma instabilities and the corresponding electron transport.

This paper analyzes the microturbulence that develops due to the mode coupling between the IITSI and ECDI in a low-temperature magnetized plasma. Theory and simulation of the kinetic instability that results from the interaction of multiple ion streams interacting with electron cyclotron dynamics are reviewed in Secs. II and III, respectively. Section IV discusses the plasma properties, and in particular, the observation of enhanced cross-field electron transport and modification of the ion distribution function resulting from the mode coupling.

**II. KINETIC INSTABILITIES**

Let us consider a partially magnetized plasma where an external electric field is applied in the  $x$  direction and a magnetic field is applied in the  $z$  direction, as shown in Fig. 1.

<sup>\*</sup>kenhara@stanford.edu<sup>†</sup>sedina.tsikata@cnrs-orleans.fr

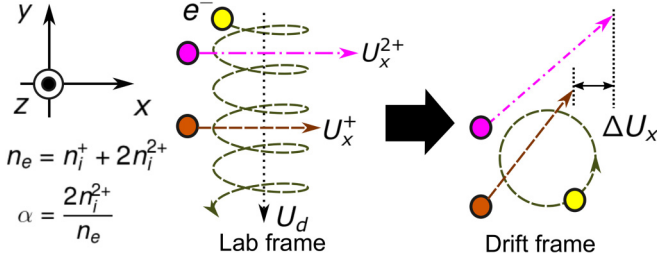


FIG. 1. A partially magnetized plasma where a DC electric field component and an external magnetic field are applied in the  $x$  and  $z$  directions, respectively. The difference between the singly charged ion velocity  $U_i^+$  and the doubly charged ion velocity  $U_i^{2+}$  in the  $x$  direction is denoted by  $\Delta U_x$ . Gyrating electrons move with an azimuthal drift,  $U_d$ , in the  $-y$  direction.

79 Nonmagnetized ions are considered and are electrostatically  
80 accelerated in the  $x$  direction while an electron drift,  $U_d$ , is  
81 formed in the  $-y$  direction. Here, two cold ion streams are  
82 considered in the  $x$  direction such that  $n_e = n_i^+ + 2n_i^{2+}$ , where  
83  $n_e$  is the electron density,  $n_i^+$  is the singly charged ion density,  
84 and  $n_i^{2+}$  is the doubly charged ion density. Here,  $\alpha = 2n_i^{2+}/n_e$   
85 is introduced, i.e.,  $n_i^+/n_e = 1 - \alpha$ .

#### A. Theory: Dispersion relation

86  
87 Assuming for the purposes of this study that the dynamics  
88 along the magnetic field are negligible ( $k_z = k_{\parallel} = 0$ ), the two-  
89 dimensional dispersion relation in the  $x$ - $y$  plane, accounting  
90 for two cold ion species and magnetized electrons [7], can be  
91 written as

$$(k_{\perp} \lambda_D)^2 \left[ 1 - \frac{(1 - \alpha) \omega_{pi}^2}{(\omega - \mathbf{k} \cdot \mathbf{U}_i^+)^2} - \frac{\alpha \omega_{pi}^2}{(\omega - \mathbf{k} \cdot \mathbf{U}_i^{2+})^2} \right] + 1 - I_0(b) \exp(-b) + \sum_{n=1}^{\infty} \frac{2\omega^2 I_n(b) \exp(-b)}{(n\omega_B)^2 - \omega^2} = 0, \quad (1)$$

92 where  $k_{\perp}^2 = k_x^2 + k_y^2$ ,  $\lambda_D = [\epsilon_0 k_B T_e / (e^2 n_0)]^{1/2}$  is the Debye  
93 length,  $\omega_{pi} = [e^2 n_0 / (m_i \epsilon_0)]^{1/2}$  is the ion plasma frequency  
94 (here,  $\epsilon_0$  is the vacuum permittivity,  $k_B$  is the Boltzmann  
95 constant,  $T_e$  is the electron temperature,  $e$  is the elementary  
96 charge,  $n_0$  is the plasma density, and  $m_i$  is the ion mass),  
97  $\omega$  and  $\mathbf{k}$  are the frequency and wave vector,  $\mathbf{U}_i^s$  is the ion  
98 bulk velocity for species  $s = +$  and  $2+$  corresponding to  
99 singly and doubly charged ions, respectively,  $b = (k_{\perp} r_L)^2$ ,  
100  $r_L = v_{\perp} / \omega_B$  is the Larmor radius [here,  $v_{\perp}$  is assumed to  
101 be the electron thermal velocity  $v_{th,e} = (k_B T_e / m_e)^{1/2}$ ,  $\omega_B =$   
102  $eB / m_e$  is the electron gyrofrequency,  $B$  is the magnetic field  
103 amplitude, and  $m_e$  is the electron mass], and  $I_n$  is the modified  
104 Bessel function of  $n$ th kind.  $I_n(b) \exp(-b)$  is also known as  
105 the scaled modified Bessel function.

106 As shown in Fig. 1, the presence of an electron drift, e.g.,  
107  $E \times B$  drift, can be accounted for by shifting the system to  
108 the frame of the electron drift. Here,  $\mathbf{k} \cdot \mathbf{U}_i^s = k_x U_x^s - k_y U_d$ ,  
109 where  $U_x$  is the drift parallel to the applied electric field and  
110  $U_d$  is the electron drift in the  $y$  direction. The wave frequency  
111 can be shifted by  $\omega - k_x U_x^+ + k_y U_d$  and Eq. (1) can be written

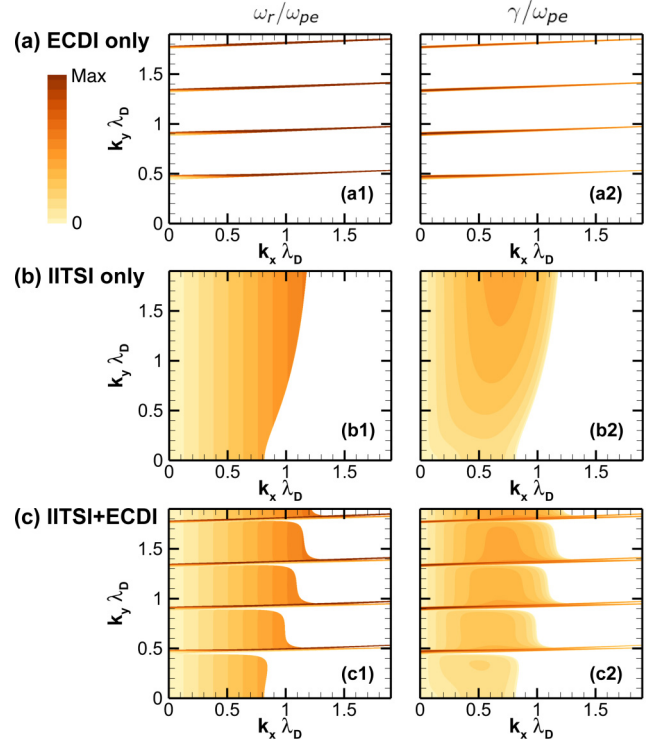


FIG. 2. Instabilities generated in a 2D partially magnetized plasma. (a) Electron cyclotron drift instability (ECDI) due to an electron drift in the  $y$  direction, where  $\tilde{U}_d = 0.239$ , assuming only singly charged ions, i.e.,  $\alpha = 0$ . (b) Ion-ion two-stream instability (IITSI) due to the mixture of singly and doubly charged ions, where  $\Delta \tilde{U}_x = 3.2 \times 10^{-3}$  and  $\tilde{U}_d = 0$ . (c) Coexisting ECDI and IITSI. Maximum value of color map is 0.002 for  $\omega_r/\omega_{pe}$  (left) and 0.001 for  $\gamma/\omega_{pe}$  (right). Xenon ions are considered. Here,  $B = 150$  G,  $T_e = 25$  eV,  $n_0 = 2 \times 10^{17} \text{ m}^{-3}$ , and  $U_x^+ = 16$  km/s.

in a normalized form as

$$\tilde{k}_{\perp}^2 \left[ 1 - \frac{\mu(1 - \alpha)}{\tilde{\omega}^2} - \frac{\mu\alpha}{(\tilde{\omega} - \tilde{k}_x \Delta \tilde{U}_x)^2} \right] + 1 - I_0(b) \exp(-b) + \sum_{n=1}^{\infty} \frac{2(\tilde{\omega} + \tilde{k}_x \tilde{U}_x^+ - \tilde{k}_y \tilde{U}_d)^2 I_n(b) \exp(-b)}{(n\tilde{\omega}_B)^2 - (\tilde{\omega} + \tilde{k}_x \tilde{U}_x^+ - \tilde{k}_y \tilde{U}_d)^2} = 0, \quad (2)$$

113 where  $\mu = m_e / m_i$  is the electron-to-ion mass ratio and  $\Delta U_x =$   
114  $U_x^{2+} - U_x^+$  is the difference between the doubly and singly  
115 charged ion velocities in the cross-field direction. The tilde  
116 quantities denote normalized parameters. Time, space, and  
117 velocity are normalized with respect to the electron plasma  
118 frequency,  $\omega_{pe} = [e^2 n_0 / (m_e \epsilon_0)]^{1/2}$ , Debye length,  $\lambda_D$ , and  
119 electron thermal speed,  $v_{th,e}$ , respectively.

120 The dispersion relation of the 2D ECDI when  $\alpha = 0$   
121 (singly charged ions only) and  $U_d \neq 0$  is shown in Fig. 2(a).  
122 The maximum growth rate is located near  $k_x = 0$ . The ECDI  
123 dispersion relation at  $k_x = 0$  is shown in Fig. 3 (cf. Ref. [7]).  
124 The 2D dispersion relation yields a resonance condition for  
125 the ECDI, namely,  $\tilde{k}_y \tilde{U}_d = n\tilde{\omega}_B$ , where  $n > 0$ . Note that the  
126 current-carrying ion-acoustic instability can be derived in the  
127 limit of zero magnetic field (i.e.,  $b \rightarrow \infty$ ) and singly charged  
128 ions (i.e.,  $\alpha = 0$ ) [32].

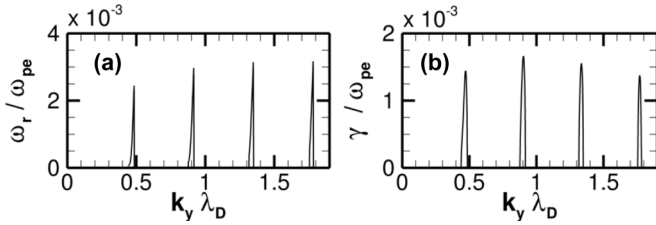


FIG. 3. ECDI dispersion relation at  $k_x \lambda_D = 0$  from Fig. 2: (a) real part of the frequency and (b) growth rate.

Figure 2(b) shows the case where the electron drift is absent, i.e.,  $U_d = 0$ , and  $\alpha$  is set at 0.5 as an illustrative case. The unstable roots (resonant condition) of the IITSI can be found at  $\tilde{k}_x < \sqrt{\mu}/\Delta\tilde{U}_x = O(1)$ . The magnetized electron contribution becomes small under this condition, reducing Eq. (2) to a dispersion relation of a two-stream instability. Since  $\tilde{U}_x^+$  is a few orders of magnitude smaller than  $\tilde{U}_d$ , the ECDI-type resonance with the axial velocity is unlikely to be observed.

Figure 2(c) illustrates the coexistence of the ECDI and IITSI. The resonances of the ECDI in 2D (narrow lobes at discrete  $k_y$  values and present for all  $k_x$ ) are apparent, along with the IITSI solutions as shown in Fig. 2(b). It can be seen that the ECDI growth rates are larger than the IITSI growth rates in the present 2D configuration since the ECDI exhibits discrete resonance-type solutions. In addition, the presence of the ECDI lobes in Fig. 2(c), while not affecting the observed IITSI mode frequencies, does reshape the unstable regions corresponding to the IITSI.

### B. Observations from experiments

The IITSI under study in this work is distinct from the ECDI, not only with regard to the instability mechanism, but also in terms of the spatial localization in laboratory cross-field discharges such as Hall effect thrusters and planar magnetrons.

In coherent Thomson scattering experiments [18,20], wave identification is performed through the measurement of electron density fluctuations. The diagnostic technique allows for the measurement of such fluctuations not only at different length scales but also along different directions, e.g., aligned primarily with the  $E \times B$  drift in studies of the ECDI or primarily along the applied electric field in studies of the IITSI.

These experiments have provided evidence (i) that both ECDI and IITSI modes, although different in their nature of excitation, are associated with density fluctuations of similar spatial scales, i.e., electron Larmor radius scales (on the order of 1 mm), (ii) that the fluctuations driven by ECDI (i.e.,  $k_y \neq 0$ ) are strongest in the region of maximum  $E \times B$  velocity and detectable further downstream due to convection, and (iii) that the fluctuations driven by IITSI (i.e.,  $k_x \neq 0$ ) are detectable not only in a spatial region overlapping the largest-amplitude ECDI fluctuations but also over a very large axial region over which the ions are accelerated. While the plasma density fluctuations are evident from measurements, it is difficult to quantify the effects of such instability-driven plasma waves on electron transport. As the following discussions will show, the

present numerical study captures such features and clarifies the dynamics of each mode.

### III. PARTICLE-IN-CELL SIMULATION OF THE PARTIALLY MAGNETIZED PLASMA

In the present paper, we focus on the physics of the coupling between ECDI and IITSI modes within the same computational framework in the literature. The computational setup to study the  $E \times B$  discharge is identical to that originally proposed by Boeuf and Garrigues [24] and used as a benchmarking test case [33]. The 2D particle-in-cell (PIC) simulation used in this paper (explicit PIC with particle and domain decomposition) is described in Ref. [33] and has been compared with other PIC codes.

Ionization occurs upstream where the electrons are trapped by the magnetic fields. The crossed electric and magnetic fields generate an  $E \times B$  drift for electrons (the source of the ECDI) and ions are accelerated electrostatically (the source of IITSI in the presence of singly and doubly charged ion streams). The ionization rate is constant in time, leading to a constant ion current density. In steady state,  $\nabla \cdot (\mathbf{j}_{i1} + \mathbf{j}_{i2}) = e(S_{i1} + 2S_{i2})$ , where  $\mathbf{j}_{ik}$  is the ion current density and  $S_{ik}$  is the ionization rate for singly ( $k = 1$ ) and doubly ( $k = 2$ ) charged ions. Defining  $\alpha_0$  to be the fraction of doubly charged ion current density, the individual source terms are assigned as  $S_{i1}/S_i = 1 - \alpha_0$  and  $S_{i2}/S_i = \alpha_0/2$ , where  $S_i(x) = S_0 \cos[\pi(x - x_M)/(x_2 - x_1)]$  is the total ionization rate,  $x_1 = 0.25$  cm,  $x_2 = 1$  cm,  $x_M = (x_1 + x_2)/2$ , and  $S_0$  is adjusted so that the total ion current density is 400 A/m<sup>2</sup>. Xenon ions are considered. Note that  $\alpha_0$  is similar but not identical to  $\alpha$  in Sec. II.

The domain size is  $L_x = 2.5$  cm and  $L_y = 1.28$  cm in the  $x$  and  $y$  direction, respectively. The magnetic field is set to  $B(x, y) = B_{\max} + B_0 \xi(x)$ , where  $\xi(x) = 1 - \exp[-0.5\{(x - x_L)/\sigma_b\}^2]$  and  $B_0 = (B_a - B_{\max})/\xi(0)$  if  $x < x_L$  and  $B_0 = (B_c - B_{\max})/\xi(x_L)$  if  $x \geq x_L$ . Here,  $x_L = 0.75$  cm,  $\sigma_b = 0.625$  cm,  $B_{\max} = 100$  G,  $B_a = 60$  G, and  $B_c = 10$  G. Intermolecular collisions, neutral atom dynamics, and transport in the  $z$  direction are neglected. The potential drop between  $x = 0$  cm and 2.4 cm is kept constant at 200 V [24,33]. The electrons are reinjected randomly in the  $y$  direction at  $x = 2.4$  cm to satisfy charge neutrality in the system, i.e.,  $\Gamma_{ec} = \Gamma_{ea} - \Gamma_{i1a} - 2\Gamma_{i2a}$ , where  $\Gamma_{ec}$  is the number of electrons reinjected from the cathode plane, and  $\Gamma_{ea}$ ,  $\Gamma_{i1a}$ , and  $\Gamma_{i2a}$  are the number of electrons, singly charged ions, and doubly charged ions absorbed at the anode plane, respectively.

The average number of particles per cell is 250 in the steady state, which shows satisfactory convergence based on the study in Ref. [33]. The grid size is 50  $\mu\text{m}$  in both directions; i.e., the number of cells is 500 and 256 in the  $x$  and  $y$  directions, respectively. The simulation utilizes a message passing interface (MPI) and the Poisson equation is solved using Hypre, a linear algebra library.

### IV. RESULTS

The effects of doubly charged ions are investigated by varying  $\alpha_0$  from 0% to 25%, which is the range of  $\text{Xe}^{2+}$  observed in  $E \times B$  discharges [34,35].

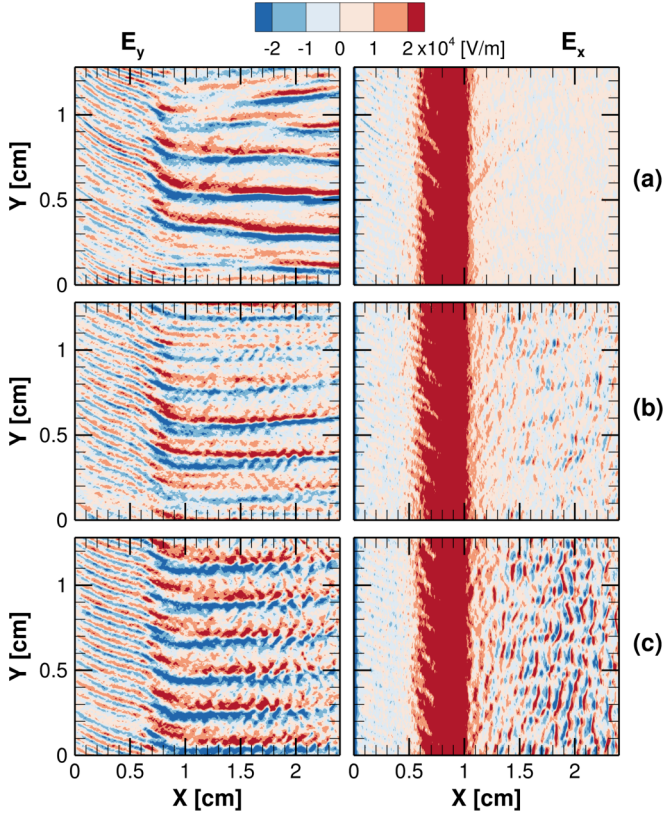


FIG. 4. Instantaneous  $E_y$  and  $E_x$  due to the cross-field plasma instabilities in the presence of singly and doubly charged ion streams. (a)  $\alpha_0 = 0$ , i.e., singly charged ions only, illustrating the ECDI in the azimuthal direction, (b)  $\alpha_0 = 10\%$  (moderate-amplitude IITSI), and (c)  $\alpha_0 = 20\%$  (large-amplitude IITSI). The axially modulated electric field develops as the fraction of doubly charged ions increases. The color bar is saturated, particularly for  $E_x$ , to allow for visualization of the plasma waves in the downstream region.

In this work, a fixed ionization rate is assumed to allow the plasma instabilities to evolve naturally and reach steady state without the need to run the simulation much longer, i.e., to resolve the slow neutral dynamics. The plasma waves driven by the instabilities achieve steady state after  $10 \mu\text{s}$  and the simulations are run up to  $30 \mu\text{s}$  (or longer) to ensure that the plasma state does not diverge. The same strategy was validated in Ref. [33] in simulations of authors from several groups. While oscillations on the order of 200 kHz (also present in benchmarking simulations in Ref. [33]) are observed in  $\alpha_0 \leq 15\%$ , such oscillations are not seen in the  $\alpha_0 = 20\%$  and  $25\%$  cases. Investigation of the low-frequency oscillations requires simulations that self-consistently model ionization and collisions, which is reserved for future work.

#### A. Coexistence of IITSI and ECDI

Figure 4 shows the instantaneous electric fields,  $E_y$  and  $E_x$ , at  $t = 18 \mu\text{s}$ , in the steady state. The results with only  $\text{Xe}^+$ , shown in Fig. 4(a), are consistent with Ref. [33]. The azimuthal plasma fluctuations, i.e.,  $E_y$ , driven by the ECDI are advected downstream. It can be seen from Figs. 4(b) and 4(c) that when  $\text{Xe}^{2+}$  is added, a cross-field (axial) mode in

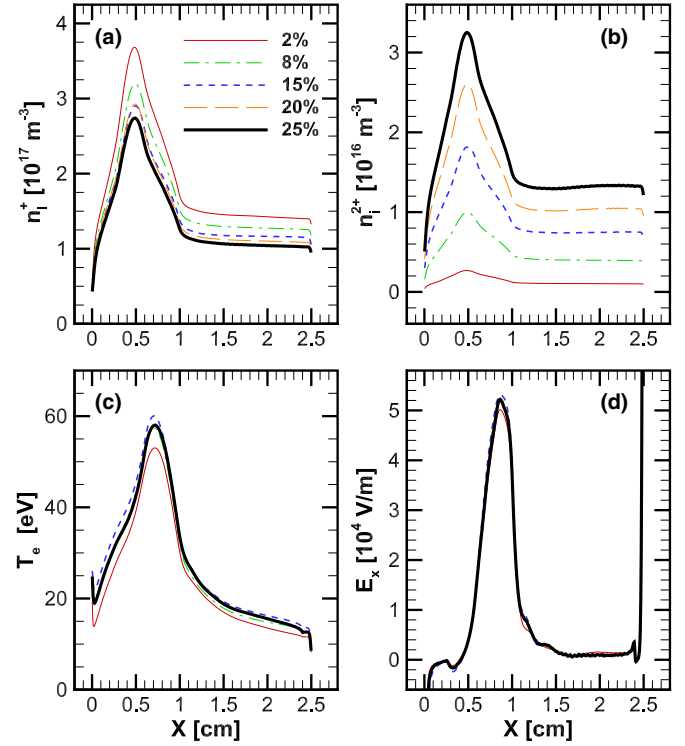


FIG. 5. Plasma properties from the simulation, averaged in the  $y$  direction and over  $5 \mu\text{s}$ . (a)  $\text{Xe}^+$  density, (b)  $\text{Xe}^{2+}$  density, (c) electron temperature, and (d) axial electric field. Ionization rate and magnetic field profiles were fixed while varying the ratio of doubly charged ionization to the total ionization rate,  $\alpha_0$ .

the  $x$  direction emerges at  $x > 1 \text{ cm}$ , where the ions are accelerated downstream. The amplitude of  $E_x$  in the downstream region increases as the doubly charged ion contribution,  $\alpha_0$ , increases. The axial fluctuation of  $E_y$  is also evident. The dominant wavelength of the  $x$  fluctuation is approximately 1 mm, which corresponds to  $k_x = 6200 \text{ rad/m}$ . Using the time-averaged,  $y$ -averaged plasma properties,  $\tilde{k}_x = k_x \lambda_D \approx 0.5\text{--}0.6$ , which is in good agreement with the theoretical dispersion relation in Fig. 2.

The results of Fig. 4 shed light on aspects concerning the two instabilities not previously accessible via experiments and linear kinetic theory analysis [20,32]. Figure 4 shows that for axial positions which coincide with those of the experimental measurements (about  $x - x_L \geq 1 \text{ cm}$ ), both the ECDI field modulation (along  $y$ ) and the IITSI field modulation (along  $x$ ) are present. Additionally, the present simulations elucidate the regions in which different instabilities are created. The ECDI is driven in the region of the fastest electron drift (approximately where  $E_x/B_z$  is largest) as expected, while the IITSI fully develops once the velocity difference  $\Delta U_x$  between the singly and doubly charged ion streams becomes large enough after acceleration. As previous experiments were only performed outside the channel in the downstream region due to restricted laser beam access, the present simulation results provide information on how the instabilities evolve in a multidimensional configuration.

The plasma properties averaged over  $5 \mu\text{s}$  and the  $y$  direction are shown in Fig. 5. The decrease of  $\text{Xe}^+$  density and

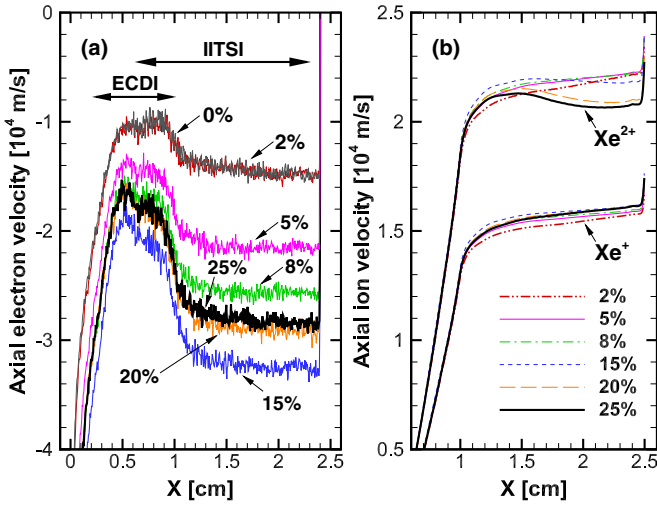


FIG. 6. Enhanced cross-field transport of electrons due to the kinetic instabilities driven by doubly charged ions. The plasma properties are averaged in the  $y$  direction and over  $5 \mu\text{s}$ , 200 sampling. (a) Electron velocity and (b) ion ( $\text{Xe}^+$  and  $\text{Xe}^{2+}$ ) velocities for various values of  $\alpha_0$ . Note that  $x = 2.4 \text{ cm}$  is where the electrons are injected in the simulation.

281 increase of  $\text{Xe}^{2+}$  density can be observed from Figs. 5(a)  
 282 and 5(b), as expected. It should be noted that there is a  
 283 slight increase in the  $\text{Xe}^{2+}$  density in the downstream region,  
 284 which is due to the deceleration caused by ion trapping due  
 285 to the wave-particle interaction. This will be discussed in  
 286 more detail shortly. Figures 5(c) and 5(d) illustrate that doubly  
 287 charged ions do not significantly alter the electron temperature  
 288 and axial electric field.

### B. Cross-field electron and ion transport

290 Figure 6(a) shows the enhancement of cross-field electron  
 291 transport by the presence of doubly charged ions in addition  
 292 to singly charged ions. Compared to cases where  $\alpha_0$  is small,  
 293 e.g.,  $\alpha_0 \leq 2\%$ , the cross-field electron transport is enhanced  
 294 by up to approximately 90% at larger  $\alpha_0$  cases. Considering a  
 295 drift-diffusion approximation for the electron transport in the  
 296 cross-field direction,

$$u_{e,\perp} = -\mu_{\perp} \left( E_{\perp} + \frac{1}{en_e} \nabla_{\perp} p_e \right), \quad (3)$$

297 where  $\mu_{\perp}$  is the cross-field mobility and  $p_e$  is the electron  
 298 pressure. Since the time-averaged plasma properties, such as  
 299  $E_{\perp}$  ( $= E_x$ ),  $n_e$ , and  $T_e$  (see Fig. 5), are not modified signifi-  
 300 cantly by  $\text{Xe}^{2+}$ , a large  $|u_{e,\perp}|$  indicates that the effective  
 301 cross-field mobility has indeed increased. While anomalous  
 302 electron transport models have been proposed, such as the  
 303 Bohm diffusion  $\mu_{\perp} = (16B)^{-1}$ , the present PIC results sug-  
 304 gest that  $\mu_{\perp}$  is dependent on the doubly charged ion frac-  
 305 tion,  $\alpha_0$ . Figure 4(c) shows that the amplitude of the plasma wave  
 306 in the downstream region becomes approximately the same in  
 307 the  $x$  and  $y$  directions, despite the fact that the growth rate of  
 308 the ECDI is an order of magnitude larger than that of the IITSI  
 309 as illustrated in Sec. II. The electric field fluctuations in both  
 310 directions enhance the cross-field transport, but not merely by

311 randomizing the electron motions, which can be inferred from  
 312 the fact that the electron temperature is not drastically changed  
 313 as shown in Fig. 5(c).

314 The enhanced electron transport across the magnetic field  
 315 lines is correlated with the coexistence of the ECDI and IITSI.  
 316 These two instabilities are generated and interact as follows:  
 317 (i) The ECDI is created in the upstream region, i.e.,  $x \sim 0.5$   
 318 cm. The plasma wave is generated due to the resonance at  
 319  $k_y \lambda_D \approx 0.9$ , where the growth rate is at maximum. However,  
 320 there is a transition to a larger wavelength mode at  $x > 0.6$  cm.  
 321 In this region, it is observed that  $k_y \lambda_D \approx 0.3$ , which is possibly  
 322 due to the physical phenomena not taken into account in the  
 323 theory. (ii) At  $0.7 \text{ cm} < x < 1 \text{ cm}$ , the ECDI and IITSI can  
 324 coexist since an azimuthal electron drift exists and the velocity  
 325 difference between  $\text{Xe}^+$  and  $\text{Xe}^{2+}$ ,  $\Delta U_x$ , increases, which can  
 326 be seen from Fig. 6(b). (iii) In the downstream region, i.e.,  
 327  $x \geq 1 \text{ cm}$ , since the azimuthal drift is small, the ECDI is  
 328 unlikely to occur. Instead, the increasing nonzero  $\Delta U_x$  further  
 329 excites the IITSI. Since the plasma wave generated by the  
 330 ECDI upstream is advected downstream, the IITSI is first  
 331 initiated in the presence of the  $k_y$  component driven by the  
 332 ECDI.

333 It can be observed from Fig. 6(a) that the electron bulk  
 334 velocity is relatively constant between  $x \in [0.5 \text{ cm}, 1 \text{ cm}]$  for  
 335 the small  $\alpha_0$  cases (0 and 2%), while its magnitude increases  
 336 over the same spatial interval (seen in the sloping trend devel-  
 337 oping over this region) in the presence of doubly charged ions  
 338 ( $\alpha_0$  exceeding 2%). This indicates that the electron mobility  
 339 is modified due to the presence of doubly charged ions. As  
 340 can be seen from Fig. 6(b), in this region, the difference  
 341 in the axial ion bulk velocities is nonzero, e.g.,  $\Delta U_x = 1\text{--}4$   
 342 km/s, and the azimuthal electron drift is nonzero, e.g.,  $U_d \approx$   
 343  $10^6 \text{ m/s}$ . With these features taken into account, it is expected  
 344 that both ECDI and IITSI modes will develop simultaneously  
 345 within this region, as discussed in Fig. 2(c).

346 The consequence of the cross-field IITSI due to the mul-  
 347 tiple ion streams (here, singly and doubly charged ions) is  
 348 that the streaming ions with different velocities thermalize and  
 349 equilibrate. This is apparent in Fig. 6(b) where the cross-field  
 350 bulk velocity of the  $\text{Xe}^{2+}$  decreases for the  $\alpha_0 = 20\%$  and  
 351  $25\%$  cases in the downstream region ( $x \geq 1.5 \text{ cm}$ ). The cross-  
 352 field plasma wave propagates with its own phase velocity and  
 353 traps, i.e., decelerates and heats, the doubly charged ions,  
 354 which is similar to the instabilities that occur within the  
 355 plasma sheath [31]. The nonlinear trapping of  $\text{Xe}^{2+}$  coincides  
 356 with the inverse tendency in the electron transport from  $\alpha_0 =$   
 357  $15\%$  to  $\alpha_0 = 20\%$  and  $25\%$ , as can be seen from Fig. 6(a).  
 358 The ion velocity distribution functions (VDFs) will be shown  
 359 later.

360 The IITSI growth rate increases monotonically as  $\alpha_0$  in-  
 361 creases for  $\alpha_0 \in [0, 0.25]$ . From an order of magnitude analy-  
 362 sis,  $\gamma / \omega_{pe} \leq O(10^{-4})$  and the characteristic time for the IITSI  
 363 to grow,  $\tau \propto \gamma^{-1}$ , is larger than  $0.1 \mu\text{s}$ . It is to be noted that  
 364 the IITSI in the present simulation is a *convective* instability.  
 365 Since the ions are advected in the  $x$  direction with a speed,  
 366  $v$ , on the order of  $10 \text{ km/s}$ , the characteristic distance for the  
 367 IITSI to grow is  $L = v\tau$ . When the growth rate of the IITSI  
 368 is small, i.e., for a small  $\alpha_0$ ,  $L$  is large. As  $\alpha_0$  increases, the IITSI  
 369 growth rate becomes large; thus,  $L \propto \gamma^{-1}$  correspondingly  
 370 decreases. Simultaneously, the plasma wave amplitude in the

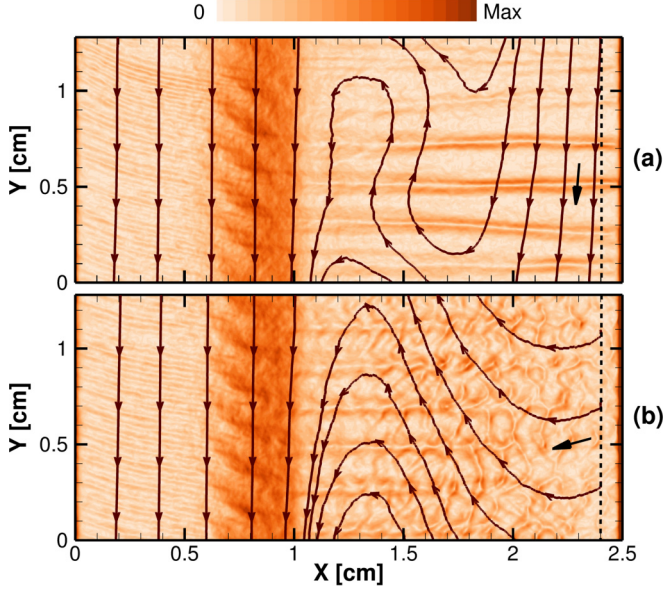


FIG. 7. Electron streamlines averaged over 1  $\mu$ s and instantaneous profile of the magnitude of electric fields,  $|\mathbf{E}| = \sqrt{E_x^2 + E_y^2}$  in Fig. 4, for the (a) ECDI and (b) ECDI and IITSI cases. Maximum value of  $|\mathbf{E}|$  is 80 kV/m. The vertical dashed line indicates the plane of electron injection. Arrows are shown to help the visualization of the electron streamline near the electron injection plane at  $x = 2.4$  cm.

axial direction, or equivalently  $E_x$ , increases for a larger  $\alpha_0$ , as shown in Fig. 4. The characteristic length over which the IITSI grows becomes on the order of a few millimeters. This can be seen also from Fig. 6(b), where the deceleration of  $\text{Xe}^{2+}$ , potentially due to the saturation of the axial wave, is apparent from  $x > 1.5$  cm for  $\alpha_0 = 20\%$  and  $25\%$ .

### C. Electron turbulent transport

Figure 7 shows the effects of the multidimensional plasma wave structures on the electron streamline to investigate the enhanced cross-field electron transport. The streamline denotes the direction of the time-averaged electron current. The ECDI-only case in Fig. 7(a) corresponds to  $\alpha_0 = 2\%$  while Fig. 7(b), showing both ECDI and IITSI, corresponds to  $\alpha_0 = 20\%$ .

One of the most notable observations from Fig. 7 is the differences in electron streamline, i.e., direction of the electron flow, near the plane of electron injection at  $x = 2.4$  cm (see the arrows in Fig. 7), despite the similarity of the averaged  $E_x$  profiles, as shown in Fig. 5(d). The temporally and spatially averaged electron flux can be written as  $\langle \Gamma_{ex} \rangle = \langle n_e E_y \rangle / B_z$  and  $\langle \Gamma_{ey} \rangle = -\langle n_e E_x \rangle / B_z$  [36,37]. Consider that plasma properties can be written as  $Q = Q_0 + Q'$ , where  $Q_0$  and  $Q'$  denote the steady-state value and fluctuation of  $Q = n_e, E_x, E_y$ . Here, the electron flux in the cross-field ( $x$ ) direction can be given as

$$\langle \Gamma_{ex} \rangle = \frac{\langle n'_e E'_y \rangle}{B_z} \quad (4)$$

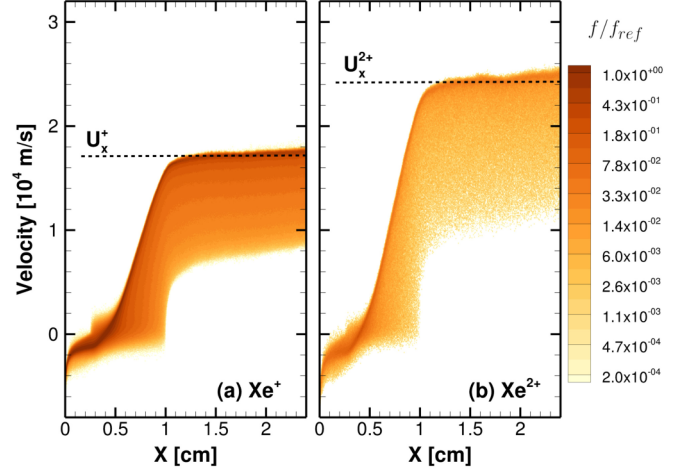


FIG. 8. The instantaneous ion velocity distribution function for  $\alpha_0 = 2\%$ , averaged over the  $y$  direction, for (a)  $\text{Xe}^+$  and (b)  $\text{Xe}^{2+}$ . The horizontal dashed lines indicate the corresponding ion velocity  $U_x^{Z+} = (ZeV_d/m_i)^{1/2}$ , where  $Z$  is the number of charges. The reference VDF value for  $\text{Xe}^+$  is chosen to be approximately the maximum value of  $\text{Xe}^+$ ,  $f_{\text{ref}} = f_{\text{max}}^+$ . Additionally,  $f_{\text{ref}} = 0.1 f_{\text{max}}^+$  is used for the VDFs of  $\text{Xe}^{2+}$ .

since  $E_{y0} = 0$  taking the average of  $E_y$  in the  $y$  direction (cf. periodic boundary condition). The electron flux in the  $y$  direction can be written as

$$\langle \Gamma_{ey} \rangle = -\frac{n_{e0} E_{x0}}{B_z} - \frac{\langle n'_e E'_x \rangle}{B_z}. \quad (5)$$

The angle bracket quantities in Eqs. (4) and (5) denote the turbulent contribution, i.e., fluctuation-based transport.

Figure 7(a) shows that  $|\langle \Gamma_{ex} \rangle| < |\langle \Gamma_{ey} \rangle|$  within  $x \in [2$  cm, 2.4 cm] where the electrons are injected. The injected electrons primarily flow in the  $-y$  direction for the ECDI-only case, which is consistent with the  $-E_{x0} \times B_z$  drift. The finite  $|\langle \Gamma_{ex} \rangle|$  indicates that azimuthal  $E_y$  fluctuations ( $k_y \neq 0$ ) induce the electron transport across the magnetic field in the absence of collisions, as discussed in Eq. (4).

In contrast, in the presence of the coupled ECDI and IITSI as shown in Fig. 7(b), electrons adopt more axial trajectories in the  $-x$  direction, indicating  $|\langle \Gamma_{ex} \rangle| > |\langle \Gamma_{ey} \rangle|$  within  $x \in [2$  cm, 2.4 cm]. The amplitude of  $E_x$  fluctuation increases and the  $E_y$  fluctuations become multidimensional, i.e.,  $k_x \neq 0$  and  $k_y \neq 0$ , in the coupled ECDI and IITSI case, as shown in Fig. 4(c). This is further evidence that the cross-field electron transport is enhanced by small-scale plasma fluctuations due to the presence of the axial plasma wave ( $k_x \neq 0$ ) in addition to the azimuthal fluctuations ( $k_y \neq 0$ ). Note that the electrons are advected in the  $+y$  direction at  $x \in [1$  cm, 1.7 cm] in Fig. 7. While such trajectories can be influenced by various drifts, including  $E \times B$ , diamagnetic, and gradient drifts [38], the cross-field electron flux is enhanced in the presence of singly and doubly charged ion streams, as shown in Fig. 6(a).

### D. Broadening of ion velocity distribution functions

Figure 8 shows instantaneous ion velocity distribution functions (VDFs) averaged over the  $y$  direction for both  $\text{Xe}^+$  and  $\text{Xe}^{2+}$ . Here,  $\alpha_0 = 2\%$ . The particles are sampled

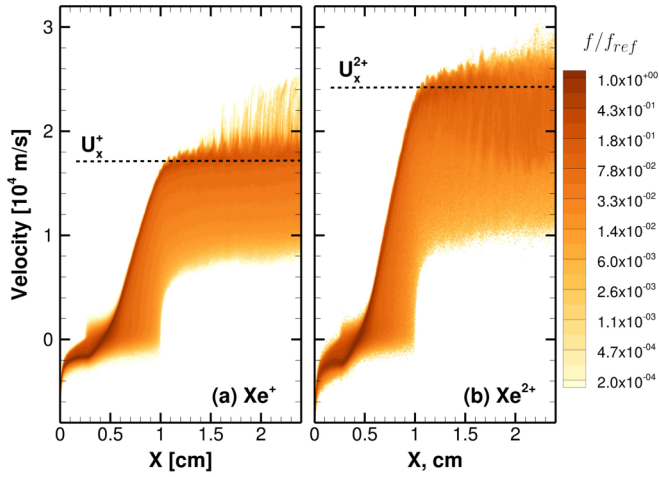


FIG. 9. Cross-field ion trapping observed in  $\alpha_0 = 20\%$  from the instantaneous ion velocity distribution function averaged over the  $y$  direction. Color map is identical to Fig. 8.

into the discretized phase space, here  $\Delta x = 5 \times 10^{-5}$  m and  $\Delta v = 100$  m/s. The ion bulk velocities obtained from the PIC simulation agree well with the values,  $U_i^+$  and  $U_i^{2+}$ , which assume a steady-state acceleration of ions across the discharge voltage,  $V_d$ . Here,  $U_x^+ \approx 1.7 \times 10^4$  m/s and  $U_x^{2+} \approx 2.4 \times 10^4$  m/s assuming a potential drop of  $V_d = 200$  V.

As shown in Fig. 8, the ion VDFs have some spread in the velocity space due to the spatial profile of the ionization rate. Such a velocity spread, i.e., nonzero ion temperature, can damp the two-stream instabilities. The electron transport at  $\alpha_0 \leq 2\%$  in our PIC simulation is indeed similar to that of the singly charged ion only case, i.e.,  $\alpha_0 = 0$ , which is illustrated in Fig. 6(a).

Figure 9 shows the ion VDFs for  $\alpha_0 = 20\%$ . While the ions form a beamlike structure for cases with smaller  $\alpha_0$  (Fig. 8) since the  $E_x$  fluctuation is small, by increasing the doubly charged ion contribution, ion trapping features now appear in both  $\text{Xe}^+$  and  $\text{Xe}^{2+}$ . The phase velocity of the plasma wave in the  $x$  direction is between  $U_x^+$  and  $U_x^{2+}$ . Perturbation of  $\text{Xe}^{2+}$  by the axial plasma wave is observed in a wide range of  $\alpha_0$  since some  $\text{Xe}^{2+}$  particles are already populated in the range of the wave velocity,  $v_\phi$ , which is between  $U_x^+$  and  $U_x^{2+}$ . The phase velocity can be estimated as  $v_\phi = \omega/k_x \approx U_x^+ + c_s$ . However, without the axial plasma wave, there are virtually no  $\text{Xe}^+$  ions in the range of  $v_\phi > U_x^+$ . Hence, the amplitude of the plasma wave must be large enough to perturb and start trapping  $\text{Xe}^+$  ions. As can be seen from Fig. 9, the trapping of both  $\text{Xe}^+$  and  $\text{Xe}^{2+}$  becomes visible at  $\alpha_0 \geq 20\%$ , which is consistent with the deceleration of doubly charged ion bulk velocity shown in Fig. 6(b). It can be considered that at this  $\alpha_0$  value,  $E_x$  (hence, the potential amplitude,  $\phi_0$ ) becomes large enough such that

$$|v_\phi - U_x^{Z+}| \geq \left( \frac{Ze\phi_0}{m_i} \right)^{1/2}, \quad (6)$$

where  $v_\phi$  is the phase velocity of the wave and  $U_x^{Z+} = (ZeV_d/m_i)^{1/2}$  is the ion beam velocity for multiply charged ion states  $Z = 1$  and 2. The right-hand side of Eq. (6) is

the trapping velocity of charged species. The results strongly indicate that the decrease in electron current from  $\alpha_0 = 15\%$  to 20%, as shown in Fig. 6(a), is correlated with the ion trapping.

These findings provide better insight into the significance of some experimental results. Broadening of the  $\text{Xe}^+$  ion distribution has been observed in laser-induced fluorescence measurements [39]. In the absence of any axial oscillations, the maximum ion velocity is  $U_i^+$ , limited by the applied DC voltage, as shown in Fig. 8. While some studies have attributed such high-energy ion formation to wave-riding effects [22,40,41], where the discharge oscillation can generate ions whose energy is larger than the applied DC voltage, the IITSI due to the mixture of  $\text{Xe}^+$  and  $\text{Xe}^{2+}$  can broaden the ion VDFs even in the absence of low-frequency discharge oscillations.

## V. DISCUSSION

As the results discussed in this paper attest, the presence of the axially propagating IITSI, coupled to the azimuthal ECDI, can influence the level of electron transport. The doubly charged ion species concentration need only be low (2% and above) for such effects to develop. The low threshold for the appearance of the IITSI, and its demonstrated effects on transport, suggest the importance of accounting for doubly charged ions in conventional low-temperature magnetized plasmas. Although we have opted to consider interaction between the two dominant ion streams in this study, triply charged xenon ions have been measured in some  $E \times B$  discharges [42] and the presence of such species may be worth accounting for as well. The formation of axial plasma waves can also be critical for ion beam spreading in the transverse (radial) direction via ponderomotive forces [43,44] and would be expected to influence macroscopic behavior in low-temperature magnetized plasmas. Understanding how the small-scale turbulence affects the large-scale self-organization, e.g., rotating spokes [45], is reserved for future work.

While the simulations performed in this paper are in 2D, here the 3D dispersion relation is discussed. The electron component in Eqs. (1) and (2) utilizes the 2D approximation ( $k_{\parallel} = 0$ ), but can be updated to account for the 3D effects ( $k_{\parallel} \neq 0$ ). The 3D dispersion relation [19,46] using normalized quantities can be written as

$$\tilde{k}^2 \left[ 1 - \frac{\mu(1-\alpha)}{\tilde{\omega}^2} - \frac{\mu\alpha}{(\tilde{\omega} - \tilde{k}_x \Delta \tilde{U}_x)^2} \right] + \tilde{\xi} \left\{ Z(\tilde{\xi}) I_0(b) e^{-b} + \sum_{n=1}^{\infty} [Z(\tilde{\xi}^+) + Z(\tilde{\xi}^-)] I_n(b) \exp(-b) \right\} + 1 = 0, \quad (7)$$

where  $k^2 = k_{\perp}^2 + k_x^2$ ,  $\tilde{\xi} = (\xi^+ + \xi^-)/2$ ,

$$\xi^{\pm} = \frac{\tilde{\omega} + \tilde{k}_x \tilde{U}_x^{\pm} - \tilde{k}_y \tilde{U}_d \pm n \tilde{\omega}_B}{\sqrt{2} \tilde{k}_z}, \quad (8)$$

and  $Z(\sigma) = \sqrt{\pi} \int \exp(-\tau) (\tau - \sigma)^{-1} d\tau$  is the plasma dispersion relation assuming a Maxwellian distribution function for electrons. In the limit of  $k_z \rightarrow 0$ , the 3D dispersion relation reduces to its 2D version, i.e., Eqs. (1) and (2).

It is known that the resonance peaks of the cyclotron motion, which are present in the 2D dispersion, become



510 smoothed in the presence of a nonzero  $k_z \lambda_D$ , leading to  
 511 a broadband ion acoustic-like spectrum. It is important to  
 512 note that the 3D ECDI is different from an ion-acoustic  
 513 instability that is derived assuming nonmagnetized electrons.  
 514 As the 3D spectra result in a broadband (nonresonant) so-  
 515 lution [19,32], the growth rates of the ECDI can become  
 516 comparable to those of the IITSI and the demarcation be-  
 517 tween the different modes which is evident in Fig. 2(c)  
 518 would be less clear. Comparison of a full 3D simulation  
 519 and the 3D linear kinetic theory is reserved for future  
 520 investigation.

## 521 VI. CONCLUSIONS

522 This paper presents insights into the cross-field electron  
 523 transport in partially magnetized plasmas due to the pres-  
 524 ence of multiply charged ions. Using a multidimensional  
 525 kinetic simulation accounting for both singly and doubly  
 526 charged ions, the nonlinear interaction between the ion-ion  
 527 two-stream instability (IITSI) and electron cyclotron drift  
 528 instability (ECDI) is investigated. The present study discusses  
 529 the effects of IITSI driven by the multiply charged ion streams  
 530 on electron and ion transport, while fixing the plasma charac-  
 531 teristics, which sets up the ECDI.

532 While it has been considered that the azimuthal plasma  
 533 wave (in the direction of  $E \times B$  drift) may be the dominant  
 534 contributor to turbulent electron transport across the magnetic  
 535 field, the present paper illustrates that the plasma wave excited  
 536 in the axial direction (parallel to the applied electric field)  
 537 and its coupling with the azimuthal ECDI further enhances  
 538 cross-field diffusion. Numerical simulations presented in this  
 539 work reveal the presence of the IITSI driven by the relative  
 540 velocity between accelerated ions of different charge states  
 541 ( $Xe^+$  and  $Xe^{2+}$  in the present study). This mode, coupled to  
 542 the ECDI via the  $E \times B$  drift of electrons, was first detected

543 using coherent Thomson scattering measurements and an ana-  
 544 lytical basis for its appearance was proposed in Ref. [20]. The  
 545 simulation results presented in this paper capture the features  
 546 of the instability studied experimentally and analytically and it  
 547 is observed that the coupling of the ECDI and IITSI enhances  
 548 the cross-field electron transport by almost 90% of the contri-  
 549 bution due to ECDI alone. Although the linear kinetic theory  
 550 predicts a growth rate for the IITSI which is smaller than  
 551 that of the ECDI, the nonlinear saturation (and, in particular,  
 552 the nonlinear coupling) of the various instabilities plays an  
 553 important role in the electron transport across the magnetic  
 554 field.

555 The plasma wave excited in the axial direction also leads  
 556 to the broadening of the ion velocity distribution functions.  
 557 Since the phase velocity of the plasma wave lies between  
 558 the velocities of the singly and doubly charged ion streams,  
 559 the trapping of doubly charged ions occurs even with small-  
 560 amplitude plasma waves in the axial direction. As the doubly  
 561 charged ion fraction increases, the amplitude of the plasma  
 562 wave driven by the IITSI increases and both the singly and  
 563 doubly charged ions become trapped by the axial plasma  
 564 wave. This leads to decrease in the bulk velocity of  $Xe^{2+}$  and  
 565 broadening of the  $Xe^+$  ion VDF.

## 566 ACKNOWLEDGMENTS

567 This material is based on work supported by the **Air Force**  
 568 **Office of Scientific Research** under Award No. FA9550-18-  
 569 1-0090 and by the **US Department of Energy, Office of**  
 570 **Science**, Office of Fusion Energy Sciences, under Award No.  
 571 DE-SC0020623. The authors acknowledge the Texas A&M  
 572 High Performance Research Computing Center. The authors  
 573 acknowledge D. Grésillon, C. Honoré, A. Héron, N. Lemoine,  
 574 and I. D. Kaganovich for prior discussions and the referees for  
 575 their valuable feedback on the manuscript.

- 
- [1] J.-P. Boeuf, *J. Appl. Phys.* **121**, 011101 (2017).  
 [2] K. Hara, *Plasma Sources Sci. Technol.* **28**, 044001 (2019).  
 [3] S. Yoshikawa and D. J. Rose, *Phys. Fluids* **5**, 334 (1962).  
 [4] D. W. Forslund, R. L. Morse, and C. W. Nielson, *Phys. Rev. Lett.* **25**, 1266 (1970).  
 [5] D. W. Forslund, R. L. Morse, and C. W. Nielson, *Phys. Rev. Lett.* **27**, 1424 (1971).  
 [6] M. Lampe, W. M. Manheimer, J. B. McBride, J. H. Orens, R. Shanny, and R. N. Sudan, *Phys. Rev. Lett.* **26**, 1221 (1971).  
 [7] S. P. Gary and J. J. Sanderson, *J. Plasma Phys.* **4**, 739 (1970).  
 [8] L. Muschietti and B. Lembège, *Adv. Space Res.* **37**, 483 (2006).  
 [9] J. McBride, E. Ott, J. Boris, and J. Orens, *Phys. Fluids* **15**, 2367 (1972).  
 [10] S. Matsukiyo and M. Scholer, *J. Geophys. Res.* **108**, 1459 (2003).  
 [11] E. R. Priest and J. J. Sanderson, *Plasma Phys.* **14**, 951 (1972).  
 [12] C. T. Dum, *Phys. Fluids* **21**, 945 (1978).  
 [13] K. Hara and C. Treece, *Plasma Sources Sci. Technol.* **28**, 055013 (2019).  
 [14] L. Muschietti and B. Lembège, *J. Geophys. Res. Space Phys.* **118**, 2267 (2013).  
 [15] J.-C. Adam, A. Héron, and G. Laval, *Phys. Plasmas* **11**, 295 (2004).  
 [16] A. Ducrocq, J.-C. Adam, A. Héron, and G. Laval, *Phys. Plasmas* **13**, 102111 (2006).  
 [17] A. Héron and J.-C. Adam, *Phys. Plasmas* **20**, 082313 (2013).  
 [18] S. Tsikata, N. Lemoine, V. Pisarev, and D. Grésillon, *Phys. Plasmas* **16**, 033506 (2009).  
 [19] J. Cavalier, N. Lemoine, G. Bonhomme, S. Tsikata, C. Honoré, and D. Grésillon, *Phys. Plasmas* **20**, 082107 (2013).  
 [20] S. Tsikata, J. Cavalier, A. Héron, C. Honoré, N. Lemoine, D. Grésillon, and D. Coulette, *Phys. Plasmas* **21**, 072116 (2014).  
 [21] S. Tsikata and T. Minea, *Phys. Rev. Lett.* **114**, 185001 (2015).  
 [22] P. Coche and L. Garrigues, *Phys. Plasmas* **21**, 023503 (2014).  
 [23] T. Lafleur, S. D. Baalrud, and P. Chabert, *Phys. Plasmas* **23**, 053503 (2016).  
 [24] J.-P. Boeuf and L. Garrigues, *Phys. Plasmas* **25**, 061204 (2018).  
 [25] S. Janhunen, A. Smolyakov, D. Sydorenko, M. Jimenez, I. D. Kaganovich, and Y. Raitses, *Phys. Plasmas* **25**, 082308 (2018).  
 [26] F. Taccogna, P. Minelli, Z. Asadi, and G. Bogopolsky, *Plasma Sources Sci. Technol.* **28**, 064002 (2019).  
 [27] S. P. Gary and N. Omidi, *J. Plasma Phys.* **37**, 45 (1987).

- [28] C. L. Grabbe, *Geophys. Res. Lett.* **12**, 483 (1985).
- [29] J.-E. Wahlund, F. R. E. Forme, H. J. Opgenoorth, M. A. L. Persson, E. V. Mishin, and A. S. Volokitin, *Geophys. Res. Lett.* **19**, 1919 (1992).
- [30] Y. Nakamura and Y. Saitou, *Plasma Phys. Controlled Fusion* **45**, 759 (2003).
- [31] S. D. Baalrud, C. C. Hegna, and J. D. Callen, *Phys. Rev. Lett.* **103**, 205002 (2009).
- [32] S. Tsikata, Ph.D. thesis, Ecole Polytechnique, 2009.
- [33] T. Charoy *et al.*, *Plasma Sources Sci. Technol.* **28**, 105010 (2019).
- [34] L. Garrigues, I. D. Boyd, and J.-P. Boeuf, *J. Propul. Power* **17**, 772 (2001).
- [35] F. S. Gulczinski, III and A. D. Gallimore, *J. Propul. Power* **17**, 418 (2001).
- [36] R. E. Waltz, *Phys. Fluids* **25**, 1269 (1982).
- [37] P. C. Liewer, *Nucl. Fusion* **25**, 543 (1985).
- [38] O. Chapurin and A. Smolyakov, *J. Appl. Phys.* **119**, 243306 (2016).
- [39] N. Dorval *et al.*, *J. Appl. Phys.* **91**, 4811 (2002).
- [40] J. Bareilles, G. J. M. Hagelaar, L. Garrigues, C. Boniface, J.-P. Boeuf, and N. Gascon, *Phys. Plasmas* **11**, 3035 (2004).
- [41] K. Hara and K. M. Hanquist, *Plasma Sources Sci. Technol.* **27**, 065004 (2018).
- [42] J. Bohlmark, M. Lattemann, J. T. Gudmundsson, A. P. Ehiasarian, Y. Aranda Gonzalvo, N. Brenning, and U. Helmersson, *Thin Solid Films* **515**, 1522 (2006).
- [43] I. D. Kaganovich, G. Shvets, E. A. Startsev, and R. C. Davidson, *Phys. Plasmas* **8**, 4180 (2001).
- [44] E. K. Tokluoglu, I. D. Kaganovich, J. A. Carlsson, K. Hara, and E. A. Startsev, *Phys. Plasmas* **25**, 052122 (2018).
- [45] R. Kawashima, K. Hara, and K. Komurasaki, *Plasma Sources Sci. Technol.* **27**, 035010 (2018).
- [46] A. Ducrocq, Ph.D. thesis, Ecole Polytechnique, 2006.